University of Nebraska - Lincoln
DigitalCommons@University of Nebraska - Lincoln

Publications, Agencies and Staff of the U.S. Department of Commerce

U.S. Department of Commerce

2014

Tracking the internal waves in the South China Sea with environmental satellite sun glint images

Bingqing Liu
Shanghai Ocean University, Shanghai, China

Hong Yang
Shanghai Ocean University, Shanghai, China

Xianwen Ding
Shanghai Ocean University, Shanghai, China

Xiaofeng Li
GST, NOAA/NESDIS, NCWCP E/RA3, College Park, MD

Follow this and additional works at: http://digitalcommons.unl.edu/usdeptcommercepub

Liu, Bingqing; Yang, Hong; Ding, Xianwen; and Li, Xiaofeng, "Tracking the internal waves in the South China Sea with environmental satellite sun glint images" (2014). *Publications, Agencies and Staff of the U.S. Department of Commerce*. 525.
http://digitalcommons.unl.edu/usdeptcommercepub/525

This Article is brought to you for free and open access by the U.S. Department of Commerce at DigitalCommons@University of Nebraska - Lincoln. It has been accepted for inclusion in Publications, Agencies and Staff of the U.S. Department of Commerce by an authorized administrator of DigitalCommons@University of Nebraska - Lincoln.

Remote Sensing Letters, 2014
Vol. 5, No. 7, 609–618, http://dx.doi.org/10.1080/2150704X.2014.949365

Taylor & Francis
Taylor & Francis Group

Tracking the internal waves in the South China Sea with environmental satellite sun glint images

Bingqing Liu[a], Hong Yang[a], Xianwen Ding[a], and Xiaofeng Li[b]*

[a]*College of Marine Sciences, Shanghai Ocean University, Shanghai, China;* [b]*GST, NOAA/NESDIS, NCWCP E/RA3, College Park, MD, USA*

(*Received 24 April 2014; accepted 22 July 2014*)

The propagation of internal solitary waves (ISWs) in the South China Sea (SCS) was tracked using National Aeronautics and Space Administration (NASA) Moderate Resolution Imaging Spectroradiometer (MODIS) and the Visible Infrared Imaging Radiometer Suite (VIIRS) sun glint image pairs. The acquisition times of the two images comprising the same pair is usually separated by about 2 hours. Four pairs of images in May and August 2013 were analysed. The ISW phase speeds were derived using the horizontal displacement of the ISW patterns and the time difference between the 2 satellite images. The phase speeds were in good agreement with the theoretical calculations using the Sturm–Louisville (S − L) equation with a non-linear term. Monthly ocean stratification data and bathymetry were used in the theoretical calculations. The ISW phase speeds are mainly affected by bottom depth, with seasonal variations. The ISWs propagated faster in August than in May. Our results also show that the ISW propagation in northern SCS can be mapped using environmental satellite sun glint images in short period of time with the advantage of large scale.

1. Introduction

Waves occur at the interface of fluids with different density. As oceanic surface waves occur at the air–sea interface, oceanic internal waves occur in the ocean interior where the seasonal or permanent thermocline exists. Internal wave often behaves in solitary wave form in the deep ocean, which is referred to as internal solitary wave (ISW). ISW produces variability in temperature, salinity, currents, sound propagation, and primary production in the water column. In the stratified ocean, the water column is usually treated as a 2-layer system. Since the density difference between the upper mixed layer and the deeper water is about 3 orders of magnitude smaller between that of the air–sea interface, ISW tends to have much larger horizontal scale (up to 200 km), bigger vertical amplitude (up to 200 m), and lower frequency than surface waves. These large-wavelength waves are difficult to measure with in situ or shipboard instruments. Remote sensing has therefore been a vital tool for ISW observations in the ocean.

Since the launch of the first meteorological satellite in the late 1960s, oceanic ISWs were among the first oceanic phenomena identified on these satellite visible images. Apel et al. (1975) first reported the coherent ISW pattern in New York Bight on the multi-spectral scanner image of Earth Resources Technology Satellite 1 (NASA, Washington, DC, USA). Later, using visible images from the Defense Meteorological Satellite Program, Fett and Rabe (1977) studied ISWs in the South China Sea (SCS). From the mid-1980s to the early 1990s, ISWs were frequently observed on the Landsat (Artale et al.

*Corresponding author. Email: Xiaofeng.Li@noaa.gov

© 2014 Taylor & Francis
This document is a U.S. government work and is not subject to copyright in the United States.

1990) and space shuttle (Zheng, Yan, and Klemas 1993) visible images. With the advance of Earth satellite technology, ISWs were more frequently observed by the modern satellite sensors, that is the Moderate Resolution Imaging Spectroradiometer (MODIS) on-board National Aeronautics and Space Administration (NASA) Terra/Aqua satellites. These modern satellite visible sensors have multiple spectral bands and high signal-to-noise ratio; therefore, false-colour composite internal wave images were generated very clearly in large area with good spatial resolution of 250 m (Jackson 2007; Bai et al. 2014).

For ISW to appear in the visible satellite images, they must occur in the sun glint region that is a function of Sun and satellite viewing angles and ocean surface wind and wave conditions. The sun glint region varies from orbit to orbit for polar orbiting satellite and day to day as the viewing angle with respect to the Sun at a fixed Earth location changes. ISW modulates the surface currents which lead to the convergence/divergence ($\nabla \cdot V$) of the current on the sea surface. The sea surface roughness zones associated with convergence/divergence are usually clearly shown in sun glint images. In the literature, the observation of an ISW was limited to one snap shot from environmental satellite, due to the nature of the orbits of the polar orbiting satellites. In general, polar orbiting satellites are launched in pairs, for example, National Oceanic and Atmospheric Administration (NOAA) KLM series and NASA MODIS series satellites. NASA MODIS series satellites consist of one morning (Terra) and one afternoon (Aqua) satellite to ensure every location on Earth is covered every 6 hours. In this orbital configuration, we may acquire more than one sun glint image at a fixed location on daily basis. Therefore, an ISW may be imaged multiple times by these environmental satellites and thus we can derive its propagation speed and study its pattern change. In the literature, similar method was also used for ocean current and eddy tracking (Legeckis, Zhu, and Chen 1999; Liu et al. 2002) with passive remote sensing images.

In this study, repeated observations of the same ISWs with large-coverage satellite visible images are available from MODIS and its follow-on sensor Visible Infrared Imaging Radiometer Suite (VIIRS) on-board the NPOESS Preparatory Project (NPP) satellite. NPP and Terra/Aqua have similar sun synchronous orbital characteristics. The difference between the Terra and NPP local passing times in the SCS is about 2 hours. This additional NPP satellite helps to improve the time intervals of the two MODIS satellites from about 6 to 2 hours. Although affected by clouds, MODIS, and VIIRS sensors are able to offset the disadvantage by their wide swath, high-temporal resolution, and the free data support. The SCS is an ideal area for the ISW study because: (1) ISWs emanate almost daily from Luzon Strait during spring tides (Liu et al. 2006); (2) the SCS has been an area of active ISW research for a few decades because the scale and amplitude of ISWs here is large; and (3) the location of the SCS is at low latitude, allowing abundant sun glint images to be acquired.

In this study, we extracted the locations of ISW packets from 4 MODIS/VIIRS image pairs acquired on 29, 31 May and 8, 10 August 2013. The sun glint areas in these 4 pairs of MODIS/VIIRS images cover the region spanning from 111° to 120° E and 17° to 24° N. Sea surface manifestations of ISWs can be delineated in this ocean area. We digitized 16 ISW pairs from these 4 pairs of images. The travelling distances of ISW packets on image pairs were tracked in a Geographic Information System (GIS) environment and their phase speeds were calculated using the travelling distance and time difference of the satellite passing times.

The internal wave wavelength, the ocean depth, and the density profile of the water column to the first order determine internal wave phase speed. By using pairs of remote sensing images, we can compare the phase speeds from the satellite measurements to the model results to better understand the propagation and evolution of these ISWs. Similar analysis method could be applied to study other oceanic phenomena: spiral eddies, equatorial waves, biogenic and oil slicks, ship wakes, among others.

2. Internal waves observed in sun glint image pairs in the SCS

2.1. Satellite sun glint images

A wide variety of oceanic and atmospheric phenomena have been observed in and around the sun glint region on optical images of the sea surface (Jackson and Alpers 2010). A sun glint region is a region from which the satellite views the mirror-like reflection from the Sun. On one hand, sun glint contaminates the sea surface temperature and ocean colour product retrievals. On the other hand, sun glint region contains valuable information on the sea surface roughness (Cox and Munk 1954). Any oceanic phenomena that modulate the sea surface roughness will leave an imprint on the sun glint images. Thus, sun glint images have been used widely in ISW (Jackson 2007), oil spill (Hu et al. 2009), and bathymetry (Shao, Li, and Li 2011) studies.

The sun glint region can be modelled well for a known satellite orbit at a specific date/time (Jackson and Alpers 2010; Zhang and Wang 2010). It is calculated using the latitude/longitude points, Sun and satellite sensor azimuth and zenith angles, and ocean surface winds. The aerosol and wind directions also contribute to the sun glint variation, but their effects are not significant (Zhang and Wang 2010). Figures 1(*a*) and (Figures 1(*b*) are 2 MODIS images acquired in the SCS on 31 and 29 May 2013, respectively. The bright patterns in the middle of the images are the sun glint areas, and the two red lines represent the sun glint boundaries for the MODIS images. In order to calculate the area of the sun glint, we first used the method of Jackson and Alpers (2010) to calculate the normalized sun glint radiance image and then applied empirical threshold value to obtain the sun glint edge pixels. After that, we applied the Canny (1986) edge detector to derive the boundaries of the sun glint. It is clear that the combination of 2 sun glint regions covers most of the SCS. We did the calculations for all 4 pairs of MODIS/VIIRS images. The ISW patterns on the MODIS image acquired on 31 May 2013 are in Figure 2(*a*) and the VIIRS image taken about 2 hours 31 minutes 12 seconds later is shown in Figure 2(*b*). One can see that there are 3 ISW packets in both images. Each packet contains several wave crests propagating towards the west with leading crest being the largest and the trailing wave crests becoming smaller. All ISW patterns on the VIIRS images appeared to the west of those on MODIS images, indicating that the ISWs propagated to the west.

2.2. Extraction of internal wave crests from sun glint images

The ISW crests can appear as bright and dark patterns in sun glint images. In the sun glint area, ISWs become visible because the sun glitter radiance depends on the surface wave spectrum modulated by the ISW-induced surface current. Optical imaging is strongly dependent upon the viewing geometry. In a sun glint image, there normally exists a critical angle: a surface feature goes through a brightness reversal (Hu et al. 2009; Jackson and Alpers 2010). Sea surface roughness variations associated with ISWs are visible on Synthetic Aperture Radar (SAR) as well as on visible images, but the dark and bright bands are ranked inversely which are also related to the polarity (Jackson and Alpers 2010). Whether ISW pattern is bright or dark in visible images depends on critical angle at the ISW location. For ISW patterns in Figure 2, the ISW packets all appeared as bright curvilinear features. We extracted these features using the same image processing procedure as given in Liu et al. (2014). The circular feature at the centre of the image is Dongsha Atoll. Thirty-two ISW packets (16 pairs) from these 4 pairs of MODIS/VIIRS images are digitized in Figure 3, and the time intervals between each pair of ISWs are given in Table 1. For easy identification in Figure 3, we name the ISW packets in the 4 image pairs alphanumerically by time and longitude (from east to west). With this notation, for example, B1, B2, B3, and

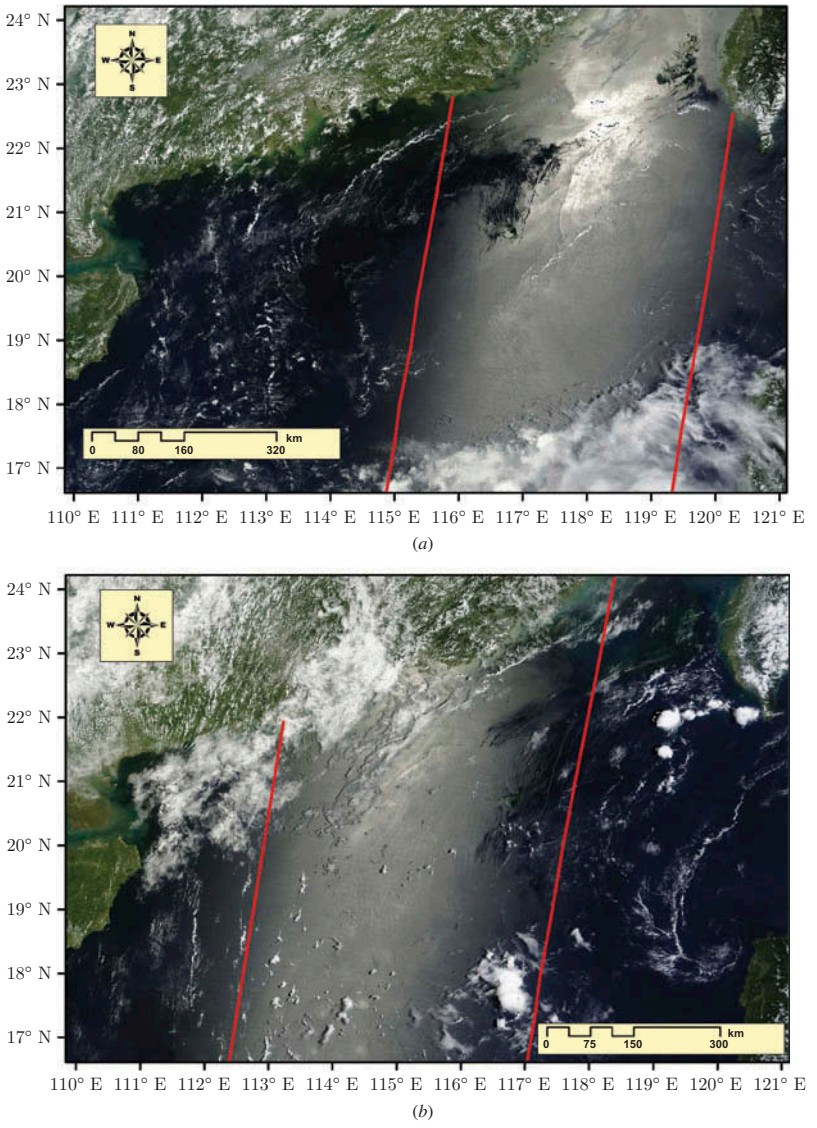

Figure 1. MODIS images acquired in the South China Sea on 31 (*a*) and 29 May (*b*), 2013. The bright areas between two red lines are the sun glint regions.

B4 are 4 ISW packets in the image pair acquired on 31 May 2013 and B1-1 is the easternmost wave crest in the easternmost wave packet. The locations of unpaired ISW wave crests and the sun glint boundaries are also plotted in Figure 3.

2.3. Spatial variation of the ISW phase speeds derived from satellite images

The extracted ISW phase speeds from satellite image pairs are given in Table 1. The average phase speed decreases from east to west significantly. Taking ISW phase speed for the easternmost packet, B1 as an example, we find that the first and second wave crests (B1-1 and B1-2) are located in the water depth of 2000–2800 m and the average phase speeds are 2.62 and 2.49 m s^{-1}, respectively. To the west of B1 in the second wave

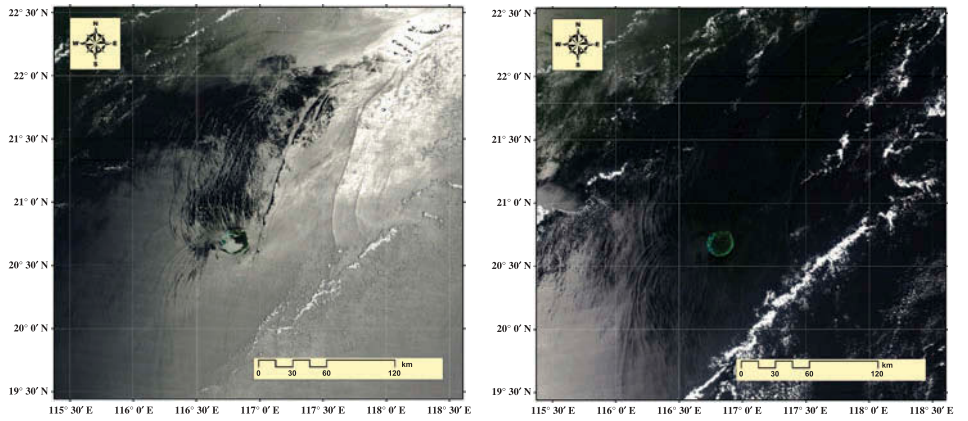

Figure 2. MODIS (*a*) and VIIRS (*b*) images acquired near Dongsha Atoll on 31 May 2013 showing westward propagation of ISW packets in the South China Sea. The leading ISW packet propagated away from Dongsha Atoll. The acquisition times of the two images are separated by about 2 hours (Table 1).

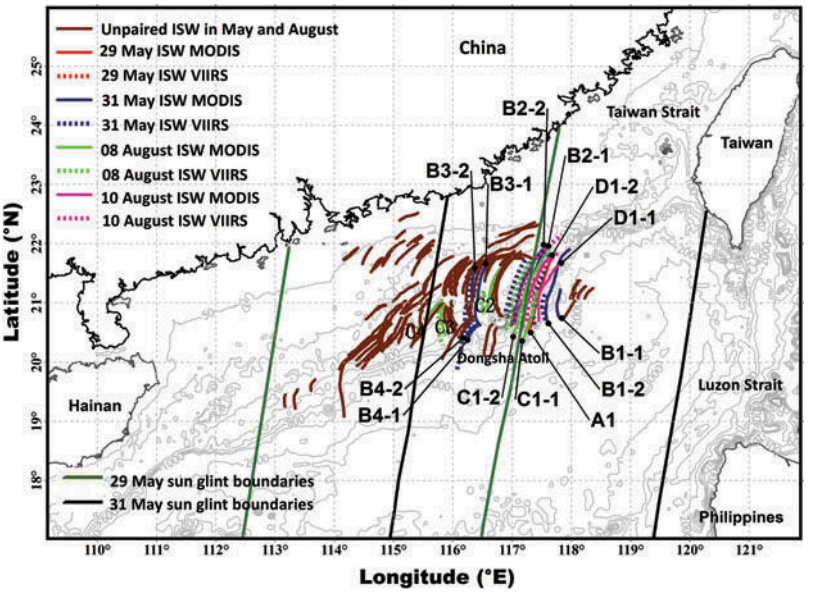

Figure 3. Locations of ISWs observed in four pairs of satellite sun glint images. The MODIS and NPP observed ISWs are shown in solid and dashed lines, respectively. Blue and red lines denote the ISWs observed in May and August 2013, respectively. The black and green lines represent the sun glint boundaries for MODIS images acquired on 29 and 31 May 2013, respectively.

packets, B2-1 and B2-2 are at the eastern edge of Dongsha Atoll and in the water depth of 1000–1500 m. The average phase speeds of B2 are much slower than those of B1. After passing the Dongsha Atoll, the northern and southern parts of the ISWs continued to propagate westwards with changing directions and speeds, interacting with each other behind the atoll. B3 and B4 are the northern and southern arms and located in the water

Table 1. Phase speeds of ISWs as measured at different locations from 4 pairs of MODIS/VIIRS images.

Date/Time	Time difference (hh:mm:ss)	Image Pair label	Wave Packet Number	Wave Crest	Water depth (m)	Average phase speed (m s^{-1})
29 May 2013 MODIS: 03:10:00 VIIRS: 04:24:20	01:14:20	A	1	1	1400–2000	2.39
31 May 2013 MODIS: 02:55:00 VIIRS 05:26:12	02:31:12	B	1	1	2000–2800	2.62
				2	2000–2800	2.49
			2	1	1000–1500	1.51
				2	1000–1500	1.60
			3	1	200–400	0.84
				2	200–400	0.83
			4	1	400–800	1.16
				2	400–800	1.14
8 August 2013 MODIS: 03:15:0 VIIRS: 05:33:30	02:18:30	C	1	1	900–1300	2.02
				2	900–1300	1.81
			2	1	250–350	0.76
			3	1	300–450	0.89
10 August 2013 MODIS: 03:00:00 VIIRS: 04:55:30	01:55:30	D	1	1	1500–2400	2.59
				2	1500–2400	2.26

depth between 300 and 800 m. The average phase speed of B3-1 and B3-2 manifest no significant difference. It is evident that the phase speeds for B3-1 and B3-2 decrease from south to north with relevant water depth decreasing by about 250 m. Further to the west, the average phase speeds of B4-1 and B4-2 are 1.14 and 1.16 m s^{-1}, respectively, which are about 0.33 m s^{-1} faster than that of northern part of B3 with the corresponding water depth increasing by about 200 m. The reason that the northern part of the ISW (B3) propagates slower than the southern part (B4) is probably because the water depth in the north is relatively shallower than that in the south of Dongsha Atoll.

The average phase speed of A1 is 2.39 m s^{-1}, the phase speeds along the A1-1 crest showed decreasing pattern from the south to the north. C1-1 and C1-2 lie to the east of the Dongsha Atoll in the water depth of 900–1300 m. The average phase speeds along C1-1 and C1-2 are 2.02 and 1.81 m s^{-1}, respectively. All the ISWs 'D' are located between 117° and 117.75°E, where the water depth spans from 1500 to 2400 m. The water depth decreases by approximately 1200 m from the south to the north along D1-2, and the corresponding ISW phase speed decreases by about 1.10 m s^{-1}.

3. Comparison of satellite-derived ISW phase speeds with theoretical values

The propagation speed of ISWs can be determined theoretically by solving the Taylor–Goldstein (T − G) equation using water depth (H), ocean stratification, and background current information (Gill 1982). Compared to water depth and ocean stratification, background current usually has a smaller influence on ISW phase speed variation. If we take the background current as zero, T − G equation can be simplified to Sturm–Louisville (S − L) equation (Gill 1982).

$$\left(\frac{d^2}{dz^2}+\frac{N^2(z)}{Ce^2}\right)W(z)=0. \tag{1}$$

Here, Ce is the eigenspeed, $N^2(z)$ is the buoyancy frequency squared, z is the vertical coordinates, and W is the vertical velocity. The actual non-linear ISW phase speed C depends upon its amplitude

$$C = Ce + 1/3\alpha\eta, \tag{2}$$

where non-linear coefficient α is taken as 0.02 s^{-1} (Zhao and Alford 2006) and η is the wave amplitude. Since the ISW amplitude is unknown, we assume it as 120 m in the deep (depths > 1000 m) and 20 m in shallow (depths < 1000 m) waters (Orr and Mignerey 2003; Liu et al. 2014).

In this study, water depth from the 1 minute ETOPO1 database (Amante and Eakins 2009) and the 15′ × 15′ monthly continuous ocean stratification data from the generalized digital environmental model (GDEM) database (Teague, Carron, and Hogan 1990) are used as inputs to solve the S − L equation numerically. Then the non-linear ISW phase speeds are solved using Equation (2).

The ISW phase speeds derived from MODIS/VIIRS in different months and the theoretical speed are plotted against water depth in Figure 4. The blue circle and red triangles represent the phase speeds derived from the MODIS/VIIRS image pairs in May and August, respectively. The theoretical phase speeds are shown as the blue and red curve for May and August, respectively.

The theoretical speeds calculated from climatological stratification and bathymetry are consistent with the results from the MODIS/VIIRS image pairs at all water depths.

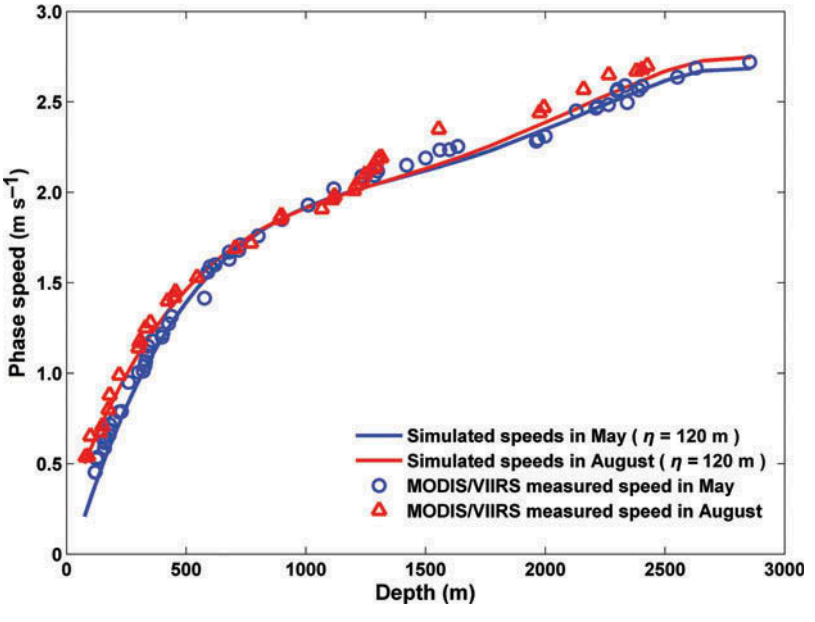

Figure 4. Comparison of ISW phase speeds from satellite images and theoretical simulations. The blue and red curves represent the theoretical phase speed derived using GDEM climatological ocean stratification data in May and August, respectively. The MODIS/VIIRS derived phase speeds are shown by scattered points as labelled.

The average phase speeds extracted from the MODIS/VIIRS pairs in May at 100–250, 250–500, 500–1000, and 1000–1500 m water depth are about 0.32, 1.01, 1.32, and 2.05 m s^{-1}, respectively. It increases to 2.20 m s^{-1} at 1500–2000 m depth. At the same water depth range (1500–2000 m), the averaged phase speed of ISW in August increases to 0.51, 1.23, 1.56, 2.21, and 2.46 m s^{-1}, respectively. It is confirmed that the phase speed derived from the August image pair is 0.2–0.3 m s^{-1} bigger than that extracted from the May image pair by MODIS/VIIRS observations and theoretical calculations. More satellite images are needed to investigate the seasonal variation in this phenomenon systematically. With better internal wave velocity estimates, there are now new opportunities to use internal wave observations to derive the ocean properties, such as mix layer depth (Li, Clemente-Colon, and Friedman 2000), *Brunt–Väisälä* frequency (Jones 1995), and heat storage (Mollo-Christensen and Mascarenhas 1979).

4. Discussions and conclusions

Four cloud-free MODIS/VIIRS image pairs were acquired in the SCS in May and August 2013 from the NASA satellites Terra and NPP, which have similar orbital characteristics. The morphology of 32 ISWs in the 4 MODIS/VIIRS image pairs was ingested into a GIS system to measure ISW–ISW horizontal displacement (Figure 3). These ISW packets are observed twice within a period of about 2 hours in each image pair (Figure 2). Therefore, the ISW phase speed can be derived from these images to yield the variation of the phase speed in northern SCS. The accuracy of this extraction method is confirmed by the comparison of ISW phase speeds from MODIS/VIIRS images with those from the S − L equation with a non-linear correction. The potential errors of this method are from inaccurate measurements from the remote sensing images. In this study, the internal wave propagation distance is estimated from MODIS and VIIRS image pair in the ArcGIS environment. The associated distance measurement error is less than 1 image pixel size (250 m). This offset does not change the ISW phase speed calculation by more than 3%. Another error source is from using the climatology stratification data to represent the instantaneous water column stratification at the satellite imaging times. However, as shown in Figure 4, the basic characteristics of internal wave propagation were captured with the monthly stratification data.

ISWs in the SCS occur as single solitary wave or in groups (trains), in which the leading wave is the largest and has the fastest phase speed (Figure 3). The phase speed in the northern SCS manifests a general decreasing trend in its westward propagation, decreasing the shoaling bottom from the east to the west and from the south to the north (Table 1). The ISW phase speeds obtained from the MODIS/VIIRS image pairs in August are greater than those in May (Figure 4). The theoretical calculations show that we underestimated the ISW phase speed in the deep ocean (>2000 m). The ISW phase speed depends upon the amplitude of the waves that is between 100 and 150 m in the study region of the SCS. However, no accurate wave amplitudes are measured in this study. We used 120 m as a representative value to plot the theoretical curves in Figure 4. Using larger or smaller values of wave amplitude will shift the curves up or down. However, this shift is very small because the non-linear correction that the ISW amplitude contributes, the 2nd term in Equation (2), is fairly small. Since α value in Equation (2) is 0.02 s^{-1}, 15 m difference in amplitude will only change the phase speed by 0.1 m s^{-1}.

In the literature, it is worth noting that SAR images have been a primary source for ISW study in the SCS (Liu and Hsu 2004; Li, Zhao, and Pichel 2008; Li, Jackson, and Pichel 2013; Liu et al. 2014; Zhao and Alford 2006; Zhao, Liu, and Li 2014). The advantage of SAR is its high spatial resolution, all-weather and day–night imaging capabilities. The

disadvantages are SAR's low-temporal resolution and small spatial coverage. In addition, SAR data are not freely and openly available at this time, although this may change when the Sentinel-1 SAR data becomes available in 6–9 months after successful launch in April 2014. Even under free and open data policy, SAR coverage is limited by the satellite operation. Tandem missions are rarely operated over the ocean. Therefore, MODIS/VIIRS sun glint images become an important free data source for ISW tracing, especially using pairs of MODIS/VIIRS separated in a few hours to estimate the phase speed of individual wave packets very accurately. The MODIS and VIIRS images are available every day and their sun glint coverage is over 500 km, which is large enough to view the entire SCS using two sun glint images separated by 2 days, that is, 29 and 31 May 2013 (see sun glint lines in Figure 3). Thus, a broader area of ISW tracing can be obtained using MODIS/VIIRS images than that using SAR image pairs and measurements from moored and shipboard instruments. Measurements from ships can provide data at different points when the ship moves and it is difficult to estimate what occurs between moorings. Thereby, the wave–wave interactions occurring when the two waves are propagating in different directions can be observed by satellites due to their large swath. In tandem MODIS/VIIRS image pairs, phase speed changes along each wave crest are easily obtained in northern SCS. In the future, the synergistic use of optical images (MODIS, VIIRS, etc.) and microwave SAR image may provide more than two observations of the same ISW in near real time.

Acknowledgements

Helpful discussion with Zhongxiang Zhao is appreciated. The views, opinions, and findings contained in this report are those of the authors and should not be construed as an official NOAA or US government position, policy, or decision.

Funding

This research was supported by the National Oceanic and Atmospheric Administration (NOAA) Ocean Remote Sensing (ORS) Program funding and the Shanghai Dongfang Scholar Program.

References

Amante, C., and B. W. Eakins. 2009. *ETOPO1 1 Arc-Minute Global Relief Model: Procedures, Data Sources and Analysis*, 19. Boulder, CO: NOAA Technical Memorandum NESDIS NGDC-24.

Apel, J. R., H. M. Byrne, J. R. Proni, and R. L. Charnell. 1975. "Observations of Oceanic Internal and Surface Waves from the Earth Resources Technology Satellite." *Journal of Geophysical Research* 80 (6): 865–871. doi:10.1029/JC080i006p00865.

Artale, V., D. Levi, S. Marullo, and R. Santoler. 1990. "Analysis of Nonlinear Internal Waves Observed by Landsat Thematic Mapper." *Journal of Geophysical Research* 95 (C9): 16065–16073. doi:10.1029/JC095iC09p16065.

Bai, X., Z. Liu, X. Li, and J. Hu. 2014. "Generation Sites of Internal Solitary Waves in the Southern Taiwan Strait Revealed by MODIS True-Colour Image Observations." *International Journal of Remote Sensing* 35 (11–12): 4086–4098. doi:10.1080/01431161.2014.916453.

Canny, J. 1986. "A Computational Approach to Edge Detection." *IEEE Transactions on Pattern Analysis and Machine Intelligence* 8 (6): 679–698. doi:10.1109/TPAMI.1986.4767851.

Cox, C., and W. Munk. 1954. "Measurement of the Roughness of the Sea Surface from Photographs of the Sun's Glitter." *Journal of the Optical Society of America* 44 (11): 838–850. doi:10.1364/JOSA.44.000838.

Fett, R., and K. Rabe. 1977. "Satellite Observation of Internal Wave Refraction in the South China Sea." *Geophysical Research Letters* 4 (5): 189–191. doi:10.1029/GL004i005p00189.

Gill, A. E. 1982. *Atmosphere-Ocean Dynamics*. London: Academic Press.

Hu, C., X. Li, W. G. Pichel, and F. E. Muller-Karger. 2009. "Detection of Natural Oil Slicks in the NW Gulf of Mexico Using MODIS Imagery." *Geophysical Research Letters* 36 (1): L01604. doi:10.1029/2008GL036119.

Jackson, C. R. 2007. "Internal Wave Detection Using the Moderate Resolution Imaging Spectroradiometer (MODIS)." *Journal of Geophysical Research* 112: C11012. doi:10.1029/2007JC004220.

Jackson, C. R., and W. Alpers. 2010. "The Role of the Critical Angle in Brightness Reversals on Sunglint Images of the Sea Surface." *Journal of Geophysical Research* 115: C09019. doi:10.1029/2009JC006037.

Jones, R. M. 1995. "On Using Ambient Internal Waves to Monitor Brunt-Väisälä Frequency." *Journal of Geophysical Research* 100 (C6): 11005–11011. doi:10.1029/95JC00139.

Legeckis, R., T. Zhu, and S. Chen. 1999. "Satellite Animations Reveal Ocean Surface Dynamics for Shortest Timescales Ever." *Eos, Transactions American Geophysical Union* 80 (20): 229–233. doi:10.1029/99EO00172.

Li, X., P. Clemente-Colon, and K. Friedman. 2000. "Estimating Oceanic Mixed Layer Depth from Internal Wave Evolution Observed from RADARSAT-1 SAR." *Johns Hopkins APL Technical Digest* 21 (1): 130–135.

Li, X., C. R. Jackson, and W. G. Pichel. 2013. "Internal Solitary Wave Refraction at Dongsha Atoll South China Sea." *Geophysical Research Letters* 40 (12): 3128–3132. doi:10.1002/grl.50614.

Li, X., Z. Zhao, and W. G. Pichel. 2008. "Internal Solitary Waves in the Northwestern South China Sea Inferred from Satellite Images." *Geophysical Research Letters* 35: L13605. doi:10.1029/2008GL034272.

Liu, A., Y. Zhao, W. E. Esaias, J. W. Campbell, and T. S. Moore. 2002. "Ocean Surface Layer Drift Revealed by Satellite Data." *Eos, Transactions American Geophysical Union* 83 (7): 61–72. doi:10.1029/2002EO000039.

Liu, A. K., and M.-K. Hsu. 2004. "Internal Wave Study in the South China Sea Using Synthetic Aperture Radar (SAR)." *International Journal of Remote Sensing* 25 (7–8): 1261–1264. doi:10.1080/01431160310001592148.

Liu, B., H. Yang, Z. Zhao, and X. Li. 2014. "Internal Solitary Wave Propagation Observed by Tandem Satellites." *Geophysical Research Letters* 41 (6): 2077–2085. doi:10.1002/2014GL059281.

Liu, C.-T., R. Pinkel, J. Klymak, M. Hsu, H.-W. Chen, and C. Villanoy. 2006. "Nonlinear Internal Waves from the Luzon Strait." *Eos, Transactions American Geophysical Union* 87 (42): 449–451. doi:10.1029/2006EO420002.

Mollo-Christensen, E., and A. D. A. S. Mascarenhas. 1979. "Heat Storage in the Oceanic Upper Mixed Layer Inferred from Landsat Data." *Science* 203 (4381): 653–654. doi:10.1126/science.203.4381.653.

Orr, M. H., and P. C. Mignerey. 2003. "Nonlinear Internal Waves in the South China Sea: Observation of the Conversion of Depression Internal Waves to Elevation Internal Waves." *Journal of Geophysical Research* 108 (C3): 3064. doi:10.1029/2001JC001163.

Shao, H., Y. Li, and L. Li. 2011. "Sun Glitter Imaging of Submarine Sand Waves on the Taiwan Banks: Determination of the Relaxation Rate of Short Waves." *Journal of Geophysical Research* 116: C06024. doi:10.1029/2010JC006798.

Teague, W. J., M. J. Carron, and P. J. Hogan. 1990. "A Comparison between the Generalized Digital Environmental Model and Levitus Climatologies." *Journal of Geophysical Research* 95: 7167–7183. doi:10.1029/JC095iC05p07167.

Zhang, H., and M. Wang. 2010. "Evaluation of Sun Glint Models Using MODIS Measurements." *Journal of Quantitative Spectroscopy & Radiative Transfer* 111 (3): 492–506. doi:10.1016/j.jqsrt.2009.10.001.

Zhao, Z., and M. H. Alford. 2006. "Source and Propagation of Internal Solitary Waves in the Northeastern South China Sea." *Journal of Geophysical Research* 111: C11012. doi:10.1029/2006JC003644.

Zhao, Z., B. Liu, and X. Li. 2014. "Internal Solitary Waves in the China Seas Observed Using Satellite Remote-Sensing Techniques: A Review and Perspectives." *International Journal of Remote Sensing* 35 (11–12): 3926–3946. doi:10.1080/01431161.2014.916442.

Zheng, Q., X.-H. Yan, and V. Klemas. 1993. "Statistical and Dynamical Analysis of Internal Waves on the Continental Shelf of the Middle Atlantic Bight from Space Shuttle Photographs." *Journal of Geophysical Research* 98 (C5): 8495–8504. doi:10.1029/92JC02955.